HeadGaS: Real-Time Animatable Head Avatars via 3D Gaussian Splatting

Helisa Dhamo   Yinyu Nie   Arthur Moreau   Jifei Song   Richard Shaw

Yiren Zhou   Eduardo Pérez-Pellitero

Huawei Noah's Ark Lab

Abstract

3D head animation has seen major quality and runtime improvements over the last few years, particularly empowered by the advances in differentiable rendering and neural radiance fields. Real-time rendering is a highly desirable goal for real-world applications. We propose HeadGaS, the first model to use 3D Gaussian Splats (3DGS) for 3D head reconstruction and animation. In this paper we introduce a hybrid model that extends the explicit representation from 3DGS with a base of learnable latent features, which can be linearly blended with low-dimensional parameters from parametric head models to obtain expression-dependent final color and opacity values. We demonstrate that HeadGaS delivers state-of-the-art results in real-time inference frame rates, which surpasses baselines by up to $2dB$, while accelerating rendering speed by over $\times 10$.

1. Introduction

Reconstructing photorealistic 3D heads which are in turn controllable and naturally expressive is essential for building digital avatars that look and behave like real humans. This has a wide range of applications including AR/VR, teleconferencing, and gaming. Designing head models that accomplish high fidelity in their appearance, are easy to capture and enable expressive control has been an active research field in recent years, specially due to the fast development of neural and differentiable rendering approaches.

Animatable 3D head reconstruction consists on driving a captured head avatar, based on a target sequence of facial expressions and head poses. In the last decades, various parametric 3D morphable models (3DMM) have emerged [4, 5, 20], which can be fitted to sequences of a moving head and later on enable pose and expression control. Though these models make it possible to drive a captured avatar via a set of low-dimensional parameters, generally their generated images lack realism. Other works utilize the fitting of low-dimensional parameters from such 3DMM models for initial estimates and build on other mechanisms to obtain more realistic imagery with animation capabilities [10, 13].
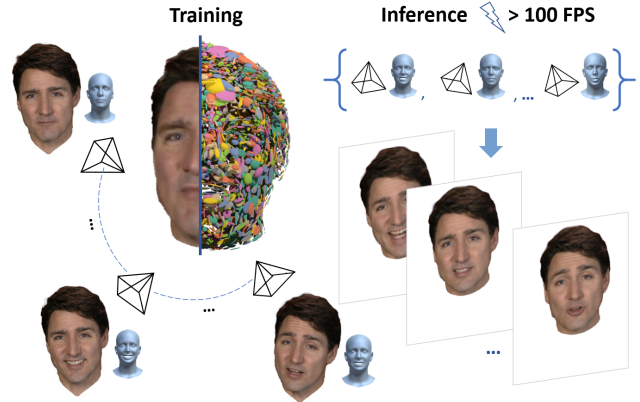

Figure 1. **Overview of HeadGaS.** We reconstruct a 3D head based on an expression-aware 3D Gaussian cloud representation, which results in real-time rendering and high image quality. **Left:** The model is trained with a monocular video of a moving head. **Right:** At inference, we query the model with a novel sequence of camera poses and expression parameters to render a real-time video.

In particular, with the recent success of differentiable rendering, various 3D-aware animatable head models emerged that can reconstruct and render 3D heads, while providing the functionality to drive them based on expression parameters from 3DMM models. These representations can be explicit (mesh, point clouds) [13, 47] or implicit (neural) [11]. Thereby, the explicit models impose stronger constraints on the head surface, which allows for better expression and pose generalization, while making it more difficult to preserve photo realism, as they inherit the limitations and artifacts of the underlying representation (mesh, point cloud) as reported in findings from other works [11] and also seen in our experiments (Fig. 3). With the recent success of neural radiance fields (NeRFs) [24], typically implicit models are based on a NeRF representation [10]. Some of these models [11, 48] prioritize time constraints and therefore rely on very fast volumetric NeRF variants (e.g. Instant NGP [25]) to enable fast training and rendering.

Despite impressive efforts to improve NeRFs to be more accurate [3] and fast [25], there is a trade-off between these

two aspects that is hard to satisfy simultaneously. Moreover, even fast and efficient NeRF models like InstantNGP typically enable interactive inference frame rates at best (10-15 fps) [17]. Very recently, 3D Gaussian Splatting (3DGS) [17] emerged as a competitive alternative to NeRF, which leads to reasonable photo-realism while bringing the rendering speed to real-time rates. This is thanks to its representation as a set of 3D Gaussian primitives, with a more efficient space coverage compared to point clouds, combined with efficient tile-based rasterization. However, in the light of 3D head animation, in its original form, 3DGS does not constitute an intuitive surface or point set that can be directly deformed based on 3DMM deformation, unlike other well-known representations *e.g.* surface or pointcloud based.

To circumvent this limitation, we propose HeadGaS, the first work that enhances 3D Gaussians with head animation capabilities (see Figure 1). At test time, our model receives a sequence of camera views and expression parameters and is capable of generating a corresponding video of the reconstructed avatar. Thereby, inspired by the expression blending idea of traditional 3DMMs [4], we introduce a base of latent features inside each Gaussian. This base is multiplied with an expression vector, and its sum is fed to a multi-layer perceptron (MLP) to yield the final color and opacity. Such model allows for varying colors of a certain rendered frame based on the expression vector. Our model can work with any 3DMM representation, as it does not explicitly model deformations with respect to a particular mesh topology. Practically, in our experiments we show that HeadGaS can be controlled with expression parameters from two different 3DMMs, namely FLAME [20] and Face-Warehouse [5]. The rendering is done in real-time frame rates, at over 100fps (more than 200fps for 512^2 resolution).

We evaluate our model in publicly monocular video datasets, also used in related works [11, 47, 48]. Thereby, we demonstrate that the proposed model is capable of producing state-of-the-art results, while increasing the rendering speed by a factor of at least $\times 10$ compared to interactive NeRF-based baselines [11, 48]. We show the applications of HeadGaS in various tasks, such as novel same-person expression transfer, cross-subject expression transfer, as well as novel view synthesis.

To summarize, our contributions include:

1. We formulate the first work that can render animatable heads on real-time, adopting an efficient set of 3D Gaussian primitives as representation.
2. We extend the 3D Gaussian representation [17] with a base of latent features, which can be weighted by an expression vector to enable head expression controllability.
3. We evaluate extensively our proposed method, and compare it against other recent state-of-the-art approaches, obtaining up to 2dB improvement and $\times 10$ speed ups.

2. Related Work

Our work consists in reconstruction and rendering of controllable 3D heads, via a set of images. As our framework relies on a radiance field, we first give an overview of the respective relevant methods. Further, we discuss works related to animatable head reconstruction.

2.1. Radiance Fields

NeRF [24] represent the scene as an implicit neural radiance field, that queries 3D space and predicts density and view-dependent color via a multi-layer perceptron (MLP). In the following years, many follow-up works have focused on improving different aspects of it such as anti-aliasing [1–3], regularization for sparse views [8, 26, 37] and speed [6, 25, 35]. DVGO [35] replace the MLP of NeRF with a density and learned feature voxel grid to considerably speed up convergence. TensoRF [6] factorize the 4D feature voxel grid of a scene into a set of low-rank 2D and 3D tensors which improves efficiency. InstantNGP [25] employ a hash grid and an occupancy grid to accelerate computation, followed by a small MLP that infers density and color. NeRFs have also been used to represent dynamic scenes including human bodies [7, 30, 39], human heads [11, 48], and generic time-varying scenes [9, 21, 28, 29, 31, 36]. Typically these models rely on a canonical space, where all observations are mapped for time consistent reconstruction. Thereby, the fastest head animation methods [11, 48] build on an InstantNGP hash grid to enable rendering in interactive frame rates (10-15 fps).

3DGS [17] represent a scene as a set of explicit 3D Gaussians with the motivation to minimize computation in empty spaces. Their efficient representation combined with tile-based rasterization algorithm allows for accelerated training and real-time rendering (over 100fps). A line of works extends the 3D Gaussian representation to model dynamic scenes [22, 40, 43]. Luiten et al. [22] propose simultaneous dynamic scene reconstruction and 6-DoF tracking by allowing the Gaussians to change position and rotation over time while enforcing the same color, size and opacity. Yang et al. [43] learn a MLP based deformation that maps 3D Gaussians to a canonical space. 4D-GS [40] propose an efficient deformation field by querying features in shared multi-resolution voxel planes. To the best of our knowledge, we are the first to propose a 3D head animation solution, and extend the explicit 3DGS representation with neural features for blending.

2.2. Head reconstruction and animation

Head reconstruction from a set of image observations has been a very active field in the recent years, including models that generalize across subjects [14, 23, 38], or rely on multi-view head captures [15, 19], which can have a static [15, 38] or dynamic form [14, 19].
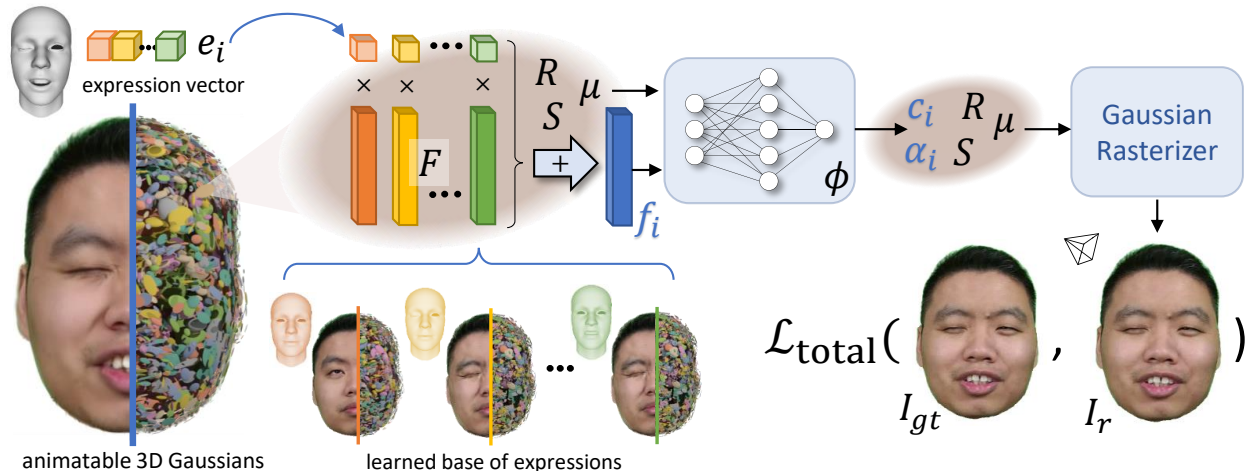
Figure 2. **HeadGaS pipeline.** We represent 3D space as a set of feature-enhanced 3D Gaussians. Every Gaussian contains a feature basis F that can be blended via the expression vector to obtain a frame specific feature f_i. The frame specific feature is fed to an MLP $\phi(\cdot)$ alongside position μ to obtain expression-dependent color c_i and opacity α_i. Finally, c_i and α_i are fed to the rasterizer alongside other Gaussian parameters like rotation R, scale S and position μ to render the image.

Most related to our proposed method, are works that learn a dynamic, animatable 3D head model from a monocular video sequence that observes the head in various poses and facial expressions, and is capable to generate a novel expression or pose at test time. A line of works rely on explicit scene representations, such as meshes or point clouds [12, 13, 18, 47]. Neural Head Avatars [13] models the geometry and texture explicitly via a hybrid representation consisting of a coarse morphable model, followed by a neural based refinement that predict voxel offsets. PointAvatar [47] propose a deformable point-based representation, where all points have the same radius. Our 3D Gaussian set shares some similarity with a point cloud, yet it is more flexible. Each Gaussian can have its own radius and different axis lengths (*i.e.* ellipsoidal shape instead of spherical).

Another line of works extend implicit neural radiance representations. NerFACE [10] use a dynamic NeRF to combine scene information with a morphable head model to enable pose and expression control. IMAvatar [46] utilizes neural implicit surfaces [27] and learns an implicit deformation field from canonical space to observation based on expression parameters and pose. With the goal of fast training, and interactive rendering, more recent works extend IntantNGP [25] with head aware models. INSTA [48] use a tracked FLAME mesh as a geometrical prior to deform the point into canonical space, followed by Instant-NGP [25]. NeRFBlendShape [11] follow a different approach, that in contrast to most previous works does not rely on deformation. Instead, inspired by classic blendshape models for heads [5], they utilize a base of multi-level hash grid fields [25], where the model can be driven via a linear blending of such hash grid base with the expression vector. Similarly AvatarMav [42] use expression weights to blend a set of motion voxel grids. Our proposed approach resembles these blending-based ideas, but instead we use the expression vector to blend latent Gaussian features to predict expression-specific color and opacity.

Different from all works discussed in this section, we adopt a set of 3D Gaussian as neural radiance representation, to take advantage of the fast rendering benefits, combined with competitive photo realism.

3. Method

Given a monocular video of a moving head, our goal is to learn a 3D head model and render novel images of this avatar based on a facial expression vector and camera pose. As a pre-processing step, similar to other works [11, 13, 47, 48], we require head poses and a vector of expression weights associated with each frame, and adopt a head tracking pipeline to achieve this. Note that HeadGaS does not explicitly build on a certain parametric model, and it can therefore work with different head models. Practically we have performed experiments with [5, 20] based on the head tracking frameworks of [11, 46, 48]. The resulting head poses are converted to camera poses. In addition, we perform video matting followed by face parsing to discard background areas and clothing to focus on the head area only. In the following sections, we will first provide some background on the vanilla 3DGS (Sec. 3.1) and further describe the proposed strategy for animatable 3DGS (Sec. 3.2), the rendering (Sec. 3.3) and its optimization (Sec. 3.4).

3.1. Vanilla 3DGS Representation

Given a set of images of a static scene and the corresponding camera poses, 3DGS [17] learn a 3D scene representation as a set of 3D gaussians, and can render a novel image from a given viewpoint. To initialize the 3D Gaussians, 3DGS utilizes a sparse point cloud, typically originating from the COLMAP [33] framework by which they also obtain the camera poses. Thereby, a 3D Gaussian is represented as a tuple of 3D covariance matrix $\mathbf{\Sigma} \in \mathbb{R}^{3 \times 3}$, Gaussian center $\boldsymbol{\mu} \in \mathbb{R}^3$, color $\boldsymbol{c} \in \mathbb{R}^{3(k+1)^2}$ and opacity $\alpha \in \mathbb{R}$, *i.e.* $\mathcal{G} = (\mathbf{\Sigma}, \boldsymbol{\mu}, \boldsymbol{c}, \alpha)$, where k is the degree of the spherical harmonics. The Gaussians are defined in world space, centered at the mean point as

$$G(x) = e^{-\frac{1}{2}(x)^T \mathbf{\Sigma}^{-1}(x)}. \tag{1}$$

To make optimization stable, *i.e.* guarantee that $\mathbf{\Sigma}$ is positive semi-definite, the covariance matrix is further decomposed into rotation and scaling:

$$\mathbf{\Sigma} = RSS^T R^T. \tag{2}$$

Color is represented via spherical harmonics (SH) with degree k and is therefore view-dependent.

The Gaussian parameters are optimized via a differentiable rasterizer, that projects the current 3D Gaussians to the image space and compares against the given ground truth images. The differentiable rasterizer relies on an efficient algorithm for sorting the Gaussians and tiling the image space, which leads to very fast training and rendering. Alongside the optimizations, 3DGS employs an adaptive mechanism for pruning and densification, to make sure that the set of gaussians represents the space effectively. For more details, we refer the reader to the 3DGS paper [17].

3.2. Feature Blending Formulation

Here we describe how we extend the 3DGS representation with animation capabilities. The vanilla 3DGS model does not inherently allow for this, as it learns a static set of parameters, which is the same for all frames. Inspired by 3DMMs, the goal of our model is to explore a blending mechanism for the 3D Gaussian components, using the pre-computed expression parameters as blending weights. Namely, we want each Gaussian to change color and opacity based on the current expression i. This leads to 3D Gaussians with dynamic appearance which occasionally appear and vanish depending on the current expression, and additionally allow color changes for non-rigid appearance effects such as wrinkles. For instance, for a certain expression vector in which the subject exhibits neutral expression with closed mouth, we want the Gaussians corresponding to lip regions to be opaque, while if the person starts to laugh, the lips become transparent and reveal the teeth regions.

The naive approach of extending a 3DGS representation to such dynamic appearance, would be to have a base of each Gaussian parameter, one for each Gaussian, and blend them based on the expression weights. However, as these values have an explicit meaning (*i.e.* color, position), a multiplication with expression weights that are not even learnable, makes this formulation limiting and prone to artifacts, as we also show in our experiments. Therefore, we extend *every* 3D Gaussian with a base of latent features $\boldsymbol{F} \in \mathbb{R}^{B \times f_{dim}}$, Figure 2. Our animatable 3D Gaussian representation then becomes $\mathcal{G}_a = (\mathbf{\Sigma}, \boldsymbol{\mu}, \boldsymbol{F})$.

The latent base is optimized together with the other parameters of the 3D Gaussian. At each iteration, we leverage the respective expression weights $\boldsymbol{e}_i \in \mathbb{R}^B$ of the current frame i, to blend the feature base $\boldsymbol{F}$ into a 1D vector $\boldsymbol{f}_i \in \mathbb{R}^{f_{dim}}$

$$\boldsymbol{f}_i = \boldsymbol{F}^T \boldsymbol{e}_i + \boldsymbol{f}_0 \tag{3}$$

where $\boldsymbol{f}_0$ is a bias term. We index with i all variables that are specific to a particular frame i. This frame specific feature $\boldsymbol{f}_i$ is then fed into a small MLP $\phi(\cdot)$, to compute the color $\boldsymbol{c}_i$ as well as the opacity α_i

$$\boldsymbol{c}_i, \alpha_i = \phi(\boldsymbol{f}_i, \psi(\boldsymbol{\mu})) \tag{4}$$

where ψ denotes cosine positional encoding.

Thereby the learned color is a 1D vector $\boldsymbol{c}_i \in \mathbb{R}^{3(k+1)^2}$, while the learned opacity is a scalar $\alpha_i \in \mathbb{R}$. Our MLP is composed of two linear layers followed by LeakyReLU activation [41], where the hidden layer has 64 channels. The last layer consists of two branches, for namely color and opacity prediction. We use a sigmoid activation function at the end of the opacity branch to constrain it to be in its natural range $[0, 1]$. As color and opacity are learned via the MLP, we omit them from the explicit Gaussian parameters.

Interestingly, though changing the centers and rotations instead, would be quite an intuitive alternative when it comes to 3D Gaussian animation, the proposed approach results in much better performance (see Sec. 4.2).

3.3. Rendering

To render frame i, we employ the respective expression $\boldsymbol{e}_i$ to populate each Gaussian with expression-dependent color and opacity. Then, the Gaussians are rendered using the camera view $\boldsymbol{W}_i$. Thereby, following [17] we employ the splatting technique [44]. Given a viewing transform $\boldsymbol{W}$ as well as the Jacobian of the affine approximation of the projective transformation $\boldsymbol{J}$, the covariance matrix $\mathbf{\Sigma}'$ in camera coordinates can be obtained from

$$\mathbf{\Sigma}' = \boldsymbol{J}\boldsymbol{W}\mathbf{\Sigma}\boldsymbol{W}^T \boldsymbol{J}^T. \tag{5}$$

The Gaussian splats are finally rendered via a tile-based differentiable rasterizer [17] that pre-sorts all primitives of an image at once.

3.4. Optimization

We initialize the 3D Gaussians centers with 2500 points. Whenever available, these points are a subset of vertices from the tracked 3DMM meshes (*e.g.* FLAME based data released by [47, 48]). As there is no mesh available for the data from [11], we sample random points within the provided near and far bounds. Empirically we found that initializing the latent features F with zeros led to the most stable solution. The model is optimized by rendering the learned Gaussians and comparing the resulting image I_r against the ground truth I_{gt}. We minimize the following loss objective

$$\mathcal{L}_{\text{total}} = \mathcal{L}_1(I_r, I_{gt}) + \lambda_s \mathcal{L}_{\text{SSIM}}(I_r, I_{gt}) + \lambda_p \mathcal{L}_p(I_r, I_{gt}) \quad (6)$$

where the λs are weighting factors and $\mathcal{L}_p$ denotes the perceptual loss [16]. We optimize using Stochastic Gradient Descent [32] with a standard exponential decay scheduling for the Gaussian position centers μ as well as the MLP.

Adaptive densification and pruning Following 3DGS [17], we combine our optimization with periodic steps of adaptive densification and pruning. First, this mechanism prunes Gaussians that are almost transparent, *i.e.* $\alpha < \tau_\alpha$ smaller than a threshold. Second, the densification targets areas that need to be populated with more Gaussians, represented with Gaussians that are too large, or regions that are too sparse and lack detail. Based on the observation that in both cases the position gradients have high values [17], the Gaussians that should be densified are identified utilizing the average gradient magnitude being above a threshold τ_{pos}. In the case of Gaussians that are too small, the objective is to increase volume and therefore the identified Gaussians are simply cloned, preserving their size. On the other hand, for Gaussians that are too large, the goal is to preserve the overall volume and therefore their scales are decreased by a factor of 1.6 after cloning, obtained empirically by [17].

3.5. Implementation details

Our learning rates for the MLP $\phi(\cdot)$, positions μ, latent features F, scale S and rotation R are namely 0.00016, 0.00016, 0.0025, 0.005 and 0.001. We set the latent feature dimensionality to $f_{dim} = 32$. All Gaussians are fed as a single batch into the MLP. The $\mathcal{L}_p$ loss is based on a VGG network [34] and has a weight of $\lambda_p = 0.1$, while $\lambda_s = 0.2$. We activate the $\mathcal{L}_p$ loss after $10k$ iterations such that it does not conflict with photometric loss at the early stage of learning. The densification starts after 500 iterations and stops with 15k iterations. In our experiments we use an SH degree of $k = 3$. We train our models on a single Tesla $V100$ GPU for $50k$ iterations taking about 1 hour.

4. Experiments

In this section we describe the evaluation protocol and the experiments carried out to evaluate the effectiveness of the proposed method. Then, we present results in three different scenarios, such as same-person pose and expression driving, novel view synthesis as well as cross-subject expression driving.

We evaluate our model on multiple datasets, made publicly available by recent works such as NeRFBlendShape (we dub this NBS data), INSTA, and PointAvatar. The NBS data [11] contains a set of monocular videos from 8 subjects, where the last 500 frames in each subject constitute the test set. The INSTA dataset [48] contains 10 subjects, where the last 350 frames of each sequence are kept as test set. We additionally evaluate on the 3 subjects made available by PointAvatar [47], where the test sets contain between $880 - 1800$ frames per subjects. For fairness of comparison, when training our method in all three datasets, we utilize the tracking data (head poses and expression weights) provided originally by the authors, such that tracking quality does not affect the comparison. We use exactly the same split as the original methods. We use a subset of about $1500 - 2500$ frames from the training set of each subject to train our model.

To assess the quality of the synthesized images we report common metrics such as Peak Signal-to-Noise Ratio (PSNR), Structural Similarity (SSIM), Learned Perceptual Image Patch Similarity (LPIPS) [45] and the Mean Squared Error (L2). Additionally, we report time measurements for the rendering in seconds. We compare against common baselines such as NeRFBlendShape [11], INSTA [48], PointAvatar [47], NHA [13], IMAvatar [46] and NeRFACE [10]. The evaluation is carried out using the respective official code repositories, as well as their official checkpoints whenever available.

4.1. Same-subject novel expression driving

In this experiment we drive the learned subjects using the novel poses and expression parameters of their test set. Table 1 reports the results of the metric comparison against baselines. The three different blocks show namely results on the data released by INSTA, NBS and PointAvatar. Figure 3 illustrates the qualitative comparison with the most recent baselines in all three datasets, namely a) INSTA data, b) NBS data and c) PointAvatar data. We observe that the proposed method outperforms all baselines on the INSTA and NBS datasets in all metrics, by namely about $1dB$ and $2dB$. Referring to Figure 3, we observe that HeadGaS leads to higher fidelity to ground truth, less artifacts, and identity preservation for all subjects. Interestingly, as INSTA relies on mesh deformations, it exhibits artifacts such as noticeable triangles (Figure 3 a), INSTA). Moreover, our model preserves better details, such as wrinkles, eyebrows, teeth
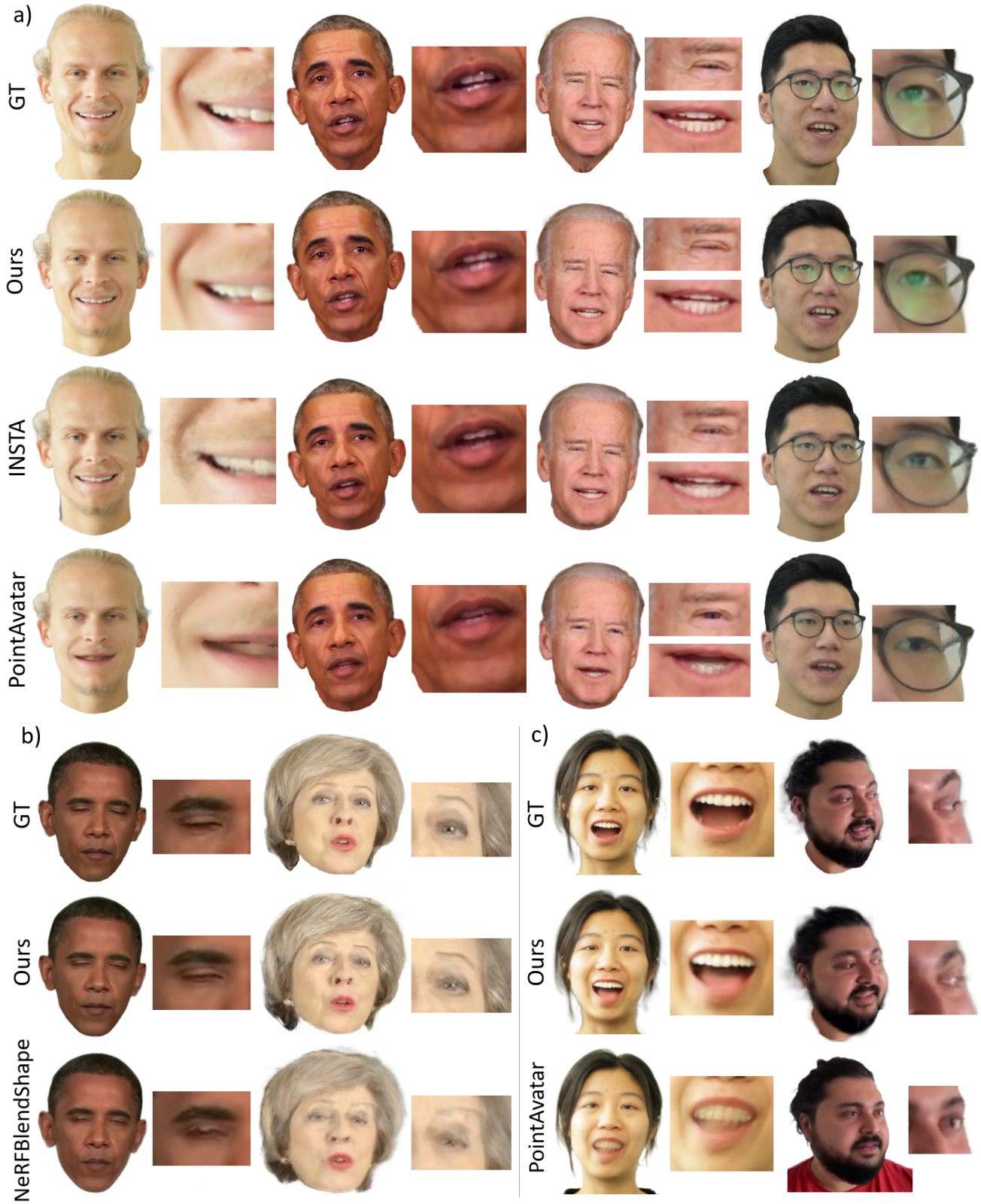
Figure 3. **Qualitative evaluation** comparing the proposed model against INSTA [48], PointAvatar [47] and NeRFBlendShape [11] baselines, namely on the **a)** INSTA data, **b)** NBS data and **c)** PointAvatar data. We provide close-ups on the right of each example, to highlight our method's ability to capture details like teeth, wrinkles and reflections.

Method	dataset	L2 ↓	PSNR ↑	SSIM ↑	LPIPS ↓	Time (s) ↓
NHA [13]		0.0024	26.99	0.942	0.043	0.63
IMAvatar [46]		0.0021	27.92	0.943	0.061	12.34
NeRFACE [10]	INSTA	0.0016	29.12	0.951	0.070	9.68
INSTA [48]		0.0017	28.61	0.944	0.047	0.05
PointAvatar [47]		0.0008	31.65	0.953	0.072	0.1 - 1.5
HeadGaS (Ours)		**0.0008**	**32.50**	**0.971**	**0.033**	**0.004**
NeRFBlendShape [11]	NBS	0.0005	34.34	0.970	0.0311	0.10
HeadGaS (Ours)		**0.0003**	**36.66**	**0.976**	**0.0261**	**0.004**
PointAvatar [47]	PointAvatar	**0.0027**	**26.04**	0.885	0.147	0.1 - 1.5
HeadGaS (Ours)		0.0039	24.79	**0.889**	**0.117**	**0.004**

Table 1. Results on the dataset provided by INSTA [48], NeRFBlendShape [11] (NBS) and PointAvatar [47]. We report PSNR, SSIM and LPIPS, together with time measures in seconds of 1 frame rendering (for 512^2 resolution).

and glass reflections, while other baselines [11, 47, 48] often struggle in such aspects. The comparison against the PointAvatar baseline shows that we are superior on the INSTA data by about $1dB$. On the PointAvatar dataset, our method surpasses the baseline in terms of LPIPS and SSIM, while having lower PSNR (1.2 dB). Overall, looking at both datasets, HeadGaS is superior to PointAvatar. Also qualitatively, we can see that PointAvatar results have distortions of some parts that undergo significant transformation (Figure 3 c)) or inaccurate teeth regions (Figure 3 b)). We believe that, as an explicit method, PointAvatar generalizes better for under-observed expressions (resulting in slightly higher PSNR). However, as these cases struggle with deformation realism, the structural metrics are worse and the problem remains unsolved. Finally, as the table shows, we surpass the rendering time of all baselines for 512 resolution by at least a factor of 10. We refer the reader to the supplementary material for more qualitative results and videos.

4.2. Ablations

In this section we ablate the HeadGaS components. First, we train a model that does not use learned features for the blending, but rather a base of colors and opacities, and uses the expression weights to obtain the final color and opacity as a weighted average. We refer to this model as *Ours w/o MLP*. In addition, since an intuitive alternative for dynamic Gaussians would be to deform the points (rather than adapting color and opacity) we introduce *Ours w/ $\Delta(\mu, R)$*, which uses the learned feature basis (and a similar MLP) to rather shift the positions μ and transform the rotations R. Further, we run a model without the perceptual loss, *i.e. Ours w/o $\mathcal{L}_p$*, to ablate its effectiveness. Additionally, to confirm the contribution of using the expression parameters as a weight for blending Gaussian features, rather than a simple condition to the MLP, we ablate a variant named *Ours w/o blending*. More details can be found in the sup-

Method	L2 ↓	PSNR ↑	SSIM ↑	LPIPS ↓
Ours w/o blending	0.0017	29.38	0.950	0.048
Ours w/ $\Delta(\mu, R)$	0.0014	29.83	0.953	0.045
Ours w/o MLP	0.0009	32.08	0.968	**0.033**
Ours w/o $\mathcal{L}_p$	0.0008	32.11	0.969	0.046
Ours	**0.0008**	**32.50**	**0.971**	**0.033**

Table 2. Ablation of HeadGaS components on the INSTA dataset.

plement. Table 2 reports the quantitative evaluation of our model components. We observe that using the expression parameters as a simple condition (*Ours w/o blending*) leads to noticeably inferior performance. Also, applying a shift to the positions and transformation to the rotations leads to worse results (*Ours w/ $\Delta(\mu, R)$*). We believe this is because transforming points is a more complex problem to optimize. Figure 4 confirms these results and reveals floater artifacts and inaccurate expressions. Further, blending the explicit parameters directly (*Ours w/o MLP*) leads to a a worse performance than our neural variant. Though the PSNR gap is not very major, we notice a drastic visual effect on the highly dynamic areas, relevant to the blending, as illustrated in Figure 4. Finally, we see that adding a perceptual loss term $\mathcal{L}_p$ leads to an improvement in most metrics.

4.3. Novel view synthesis

In Figure 5 we show our generated avatars from multiple views, including the original test set camera (left) and two additional viewpoints (right). Thereby we render the same facial expression. We observe that our model can deliver expressions that are consistent across different views.

4.4. Cross-subject expression driving

So far we have shown that our model is capable of generalizing to novel expression parameters corresponding to
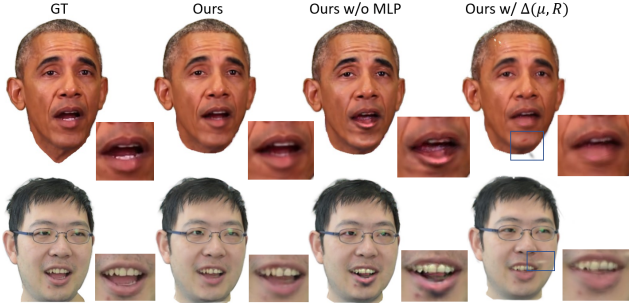
Figure 4. **Qualitative ablation on the INSTA data** illustrating the effect of MLP and the Gaussian deformation alternative.
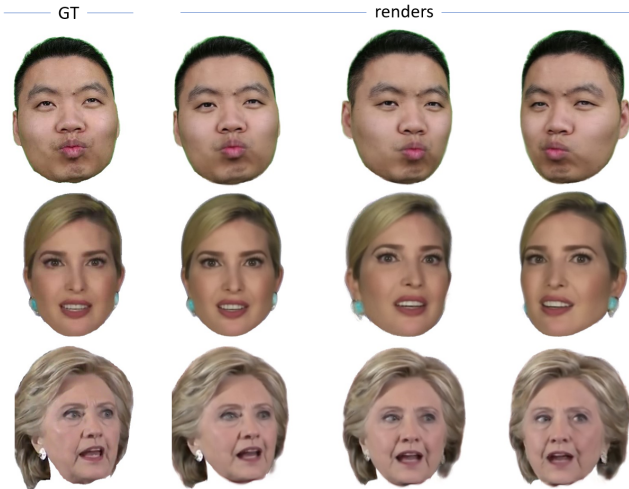

Figure 5. Qualitative HeadGaS results on multiple camera views for the same expression parameters.

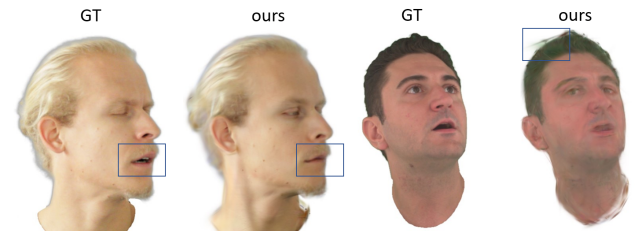Figure 6. Cross-subject expression driving.

Figure 7. **Limitations.** *Left:* subject only observed in neutral expression in non-frontal view. *Right:* Camera view that is far from the training observations.

the same person, in time-frames not observed during training. Figure 6 complements these results with cross-subject driving, *i.e.* use the facial expression from another (ground truth) source subject to drive a target subject. As can be seen in the figure, our model is capable of transferring expression across different subjects at a reasonable quality.

5. Limitations and ethical consideration

As a method that relies on tracked data, *i.e.* head poses and expressions, HeadGaS is affected by failures of the head tracker. This can take the form of inaccurate facial expressions, or blurriness in case of pose inaccuracy in the training data (Figure 7). Further, as a data driven method, HeadGaS requires a reasonable coverage of expressions spread among different views. For instance, if a head changes pose only in neutral expression, and diverse expressions are captured only in frontal view, it would be difficult to capture a non-neutral expression from side view (Figure 7, left).

We carried out this work with subjects which are pub-

licly available [11, 47, 48]. They are a combination of lab captures and public YouTube videos. We have not captured additional subjects. The authors claim that the subjects have given their consent for using their data for research purposes. The goal of this work is to immerse user experience in AR/VR applications, in which they have full control of their data and animation. However, we acknowledge that our method could be extended to generate fake content of people, without their consent, with the purpose to spread false information. We strictly oppose such behaviour.

6. Conclusion

We presented HeadGaS, a model for animatable head reconstruction and rendering from a monocular video that renders on real-time. Our extensive evaluation showed that the proposed model results in state-of-the-art performance, surpassing the baselines, while rendering on real-time frame rates (over 200fps for 512^2 resolution). We justified our design choices via a set of ablations, where we demonstrated that linearly blending implicit features leads to less artifacts than the alternative of blending explicit parameters directly. Moreover, we have shown that changing colors and opacity is more effective than the intuitive alternative of deforming the Gaussian mean positions.

References

[1] Jonathan T. Barron, Ben Mildenhall, Matthew Tancik, Peter Hedman, Ricardo Martin-Brualla, and Pratul P. Srinivasan. Mip-nerf: A multiscale representation for anti-aliasing neural radiance fields. In *Proceedings of the IEEE/CVF International Conference on Computer Vision (ICCV)*, 2021. 2

[2] Jonathan T. Barron, Ben Mildenhall, Dor Verbin, Pratul P. Srinivasan, and Peter Hedman. Mip-nerf 360: Unbounded anti-aliased neural radiance fields. *CVPR*, 2022.

[3] Jonathan T. Barron, Ben Mildenhall, Dor Verbin, Pratul P. Srinivasan, and Peter Hedman. Zip-nerf: Anti-aliased grid-based neural radiance fields. *ICCV*, 2023. 1, 2

[4] Volker Blanz and Thomas Vetter. A morphable model for the synthesis of 3d faces. In *Proceedings of the 26th Annual Conference on Computer Graphics and Interactive Techniques*, page 187–194, USA, 1999. ACM Press/Addison-Wesley Publishing Co. 1, 2

[5] Chen Cao, Yanlin Weng, Shun Zhou, Yiying Tong, and Kun Zhou. Facewarehouse: A 3d facial expression database for visual computing. *IEEE Transactions on Visualization and Computer Graphics*, 20(3):413–425, 2014. 1, 2, 3, 11

[6] Anpei Chen, Zexiang Xu, Andreas Geiger, Jingyi Yu, and Hao Su. Tensorf: Tensorial radiance fields. In *European Conference on Computer Vision (ECCV)*, 2022. 2

[7] Jianchuan Chen, Ying Zhang, Di Kang, Xuefei Zhe, Linchao Bao, Xu Jia, and Huchuan Lu. Animatable neural radiance fields from monocular rgb videos. *ArXiv*, abs/2106.13629, 2021. 2

[8] Kangle Deng, Andrew Liu, Jun-Yan Zhu, and Deva Ramanan. Depth-supervised NeRF: Fewer views and faster training for free. In *Proceedings of the IEEE/CVF Conference on Computer Vision and Pattern Recognition (CVPR)*, 2022. 2

[9] Yilun Du, Yinan Zhang, Hong-Xing Yu, Joshua B. Tenenbaum, and Jiajun Wu. Neural radiance flow for 4d view synthesis and video processing. In *Proceedings of the IEEE/CVF International Conference on Computer Vision*, 2021. 2

[10] Guy Gafni, Justus Thies, Michael Zollhöfer, and Matthias Nießner. Dynamic neural radiance fields for monocular 4d facial avatar reconstruction. In *Proceedings of the IEEE/CVF Conference on Computer Vision and Pattern Recognition (CVPR)*, pages 8649–8658, 2021. 1, 3, 5, 7

[11] Xuan Gao, Chenglai Zhong, Jun Xiang, Yang Hong, Yudong Guo, and Juyong Zhang. Reconstructing personalized semantic facial nerf models from monocular video. *ACM Transactions on Graphics (Proceedings of SIGGRAPH Asia)*, 41(6), 2022. 1, 2, 3, 5, 6, 7, 8, 11, 13

[12] Pablo Garrido, Levi Valgaerts, Ole Rehmsen, Thorsten Thormählen, Patrick Pérez, and Christian Theobalt. Automatic face reenactment. *2014 IEEE Conference on Computer Vision and Pattern Recognition*, 2014. 3

[13] Philip-William Grassal, Malte Prinzler, Titus Leistner, Carsten Rother, Matthias Nießner, and Justus Thies. Neural head avatars from monocular rgb videos. *CVPR*, 2022. 1, 3, 5, 7

[14] Yang Hong, Bo Peng, Haiyao Xiao, Ligang Liu, and Juyong Zhang. Headnerf: A real-time nerf-based parametric head model. In *IEEE/CVF Conference on Computer Vision and Pattern Recognition (CVPR)*, 2022. 2

[15] Youngkyoon Jang, Jiali Zheng, Jifei Song, Helisa Dhamo, Eduardo Pérez-Pellitero, Thomas Tanay, Matteo Maggioni, Richard Shaw, Sibi Catley-Chandar, Yiren Zhou, Jiankang Deng, Ruijie Zhu, Jiahao Chang, Ziyang Song, Jiahuan Yu, Tianzhu Zhang, Khanh-Binh Nguyen, Joon-Sung Yang, Andreea Dogaru, Bernhard Egger, Heng Yu, Aarush Gupta, Joel Julin, László A. Jeni, Hyeseong Kim, Jungbin Cho, Dosik Hwang, Deukhee Lee, Doyeon Kim, Dongseong Seo, SeungJin Jeon, YoungDon Choi, Jun Seok Kang, Ahmet Cagatay Seker, Sang Chul Ahn, Ales Leonardis, and Stefanos Zafeiriou. Vschh 2023: A benchmark for the view synthesis challenge of human heads. In *Proceedings of the IEEE/CVF International Conference on Computer Vision (ICCV) Workshops*, 2023. 2

[16] Justin Johnson, Alexandre Alahi, and Li Fei-Fei. Perceptual losses for real-time style transfer and super-resolution. In *European Conference on Computer Vision*, 2016. 5

[17] Bernhard Kerbl, Georgios Kopanas, Thomas Leimkühler, and George Drettakis. 3d gaussian splatting for real-time radiance field rendering. *ACM Transactions on Graphics*, 42 (4), 2023. 2, 4, 5

[18] Hyeongwoo Kim, Pablo Garrido, Ayush Tewari, Weipeng Xu, Justus Thies, Matthias Nießner, Patrick Pérez, Christian Richardt, Michael Zollöfer, and Christian Theobalt. Deep video portraits. *ACM Transactions on Graphics (TOG)*, 37 (4):163, 2018. 3

[19] Tobias Kirschstein, Shenhan Qian, Simon Giebenhain, Tim Walter, and Matthias Nießner. Nersemble: Multi-view radiance field reconstruction of human heads. *ACM Trans. Graph.*, 42(4), 2023. 2

[20] Tianye Li, Timo Bolkart, Michael. J. Black, Hao Li, and Javier Romero. Learning a model of facial shape and expression from 4D scans. *ACM Transactions on Graphics, (Proc. SIGGRAPH Asia)*, 36(6), 2017. 1, 2, 3, 11

[21] Zhengqi Li, Simon Niklaus, Noah Snavely, and Oliver Wang. Neural scene flow fields for space-time view synthesis of dynamic scenes. In *Proceedings of the IEEE/CVF Conference on Computer Vision and Pattern Recognition (CVPR)*, 2021. 2

[22] Jonathon Luiten, Georgios Kopanas, Bastian Leibe, and Deva Ramanan. Dynamic 3d gaussians: Tracking by persistent dynamic view synthesis. *arXiv*, 2308.09713, 2023. 2

[23] Marko Mihajlovic, Aayush Bansal, Michael Zollhoefer, Siyu Tang, and Shunsuke Saito. KeypointNeRF: Generalizing image-based volumetric avatars using relative spatial encoding of keypoints. In *European conference on computer vision*, 2022. 2

[24] Ben Mildenhall, Pratul P. Srinivasan, Matthew Tancik, Jonathan T. Barron, Ravi Ramamoorthi, and Ren Ng. Nerf: Representing scenes as neural radiance fields for view synthesis. In *ECCV*, 2020. 1, 2

[25] Thomas Müller, Alex Evans, Christoph Schied, and Alexander Keller. Instant neural graphics primitives with a multires-

olution hash encoding. *ACM Trans. Graph.*, 41(4):102:1–102:15, 2022. 1, 2, 3

[26] Michael Niemeyer, Jonathan T. Barron, Ben Mildenhall, Mehdi S. M. Sajjadi, Andreas Geiger, and Noha Radwan. Regnerf: Regularizing neural radiance fields for view synthesis from sparse inputs. In *Proc. IEEE Conf. on Computer Vision and Pattern Recognition (CVPR)*, 2022. 2

[27] Jeong Joon Park, Peter Florence, Julian Straub, Richard Newcombe, and Steven Lovegrove. Deepsdf: Learning continuous signed distance functions for shape representation. In *The IEEE Conference on Computer Vision and Pattern Recognition (CVPR)*, 2019. 3

[28] Keunhong Park, Utkarsh Sinha, Jonathan T. Barron, Sofien Bouaziz, Dan B Goldman, Steven M. Seitz, and Ricardo Martin-Brualla. Nerfies: Deformable neural radiance fields. In *Proceedings of the IEEE International Conference on Computer Vision (ICCV)*, 2021. 2

[29] Keunhong Park, Utkarsh Sinha, Peter Hedman, Jonathan T. Barron, Sofien Bouaziz, Dan B Goldman, Ricardo Martin-Brualla, and Steven M. Seitz. Hypernerf: A higher-dimensional representation for topologically varying neural radiance fields. *ACM Trans. Graph.*, 40(6), 2021. 2

[30] Sida Peng, Junting Dong, Qianqian Wang, Shangzhan Zhang, Qing Shuai, Xiaowei Zhou, and Hujun Bao. Animatable neural radiance fields for modeling dynamic human bodies. In *ICCV*, 2021. 2

[31] Albert Pumarola, Enric Corona, Gerard Pons-Moll, and Francesc Moreno-Noguer. D-nerf: Neural radiance fields for dynamic scenes. *CVPR*, 2020. 2

[32] Sebastian Ruder. An overview of gradient descent optimization algorithms. *arXiv preprint arXiv:1609.04747*, 2016. 5

[33] Johannes Lutz Schönberger and Jan-Michael Frahm. Structure-from-motion revisited. In *Conference on Computer Vision and Pattern Recognition (CVPR)*, 2016. 4

[34] Karen Simonyan and Andrew Zisserman. Very deep convolutional networks for large-scale image recognition. In *International Conference on Learning Representations*, 2015. 5

[35] Cheng Sun, Min Sun, and Hwann-Tzong Chen. Direct voxel grid optimization: Super-fast convergence for radiance fields reconstruction. In *CVPR*, 2022. 2

[36] Edgar Tretschk, Ayush Tewari, Vladislav Golyanik, Michael Zollhöfer, Christoph Lassner, and Christian Theobalt. Non-rigid neural radiance fields: Reconstruction and novel view synthesis of a dynamic scene from monocular video. In *IEEE International Conference on Computer Vision (ICCV)*. IEEE, 2021. 2

[37] Prune Truong, Marie-Julie Rakotosaona, Fabian Manhardt, and Federico Tombari. Sparf: Neural radiance fields from sparse and noisy poses. IEEE/CVF Conference on Computer Vision and Pattern Recognition, CVPR, 2023. 2

[38] Daoye Wang, Prashanth Chandran, Gaspard Zoss, Derek Bradley, and Paulo F. U. Gotardo. Morf: Morphable radiance fields for multiview neural head modeling. In *SIGGRAPH '22: Special Interest Group on Computer Graphics and Interactive Techniques Conference*. ACM, 2022. 2

[39] Chung-Yi Weng, Brian Curless, Pratul P. Srinivasan, Jonathan T. Barron, and Ira Kemelmacher-Shlizerman. HumanNeRF: Free-viewpoint rendering of moving people from monocular video. In *Proceedings of the IEEE/CVF Conference on Computer Vision and Pattern Recognition (CVPR)*, pages 16210–16220, 2022. 2

[40] Guanjun Wu, Taoran Yi, Jiemin Fang, Lingxi Xie, Xiaopeng Zhang, Wei Wei, Wenyu Liu, Qi Tian, and Xinggang Wang. 4d gaussian splatting for real-time dynamic scene rendering. *arXiv*, 2310.08528, 2023. 2

[41] Bing Xu, Naiyan Wang, Tianqi Chen, and Mu Li. Empirical evaluation of rectified activations in convolutional network. 2015. 4

[42] Yuelang Xu, Lizhen Wang, Xiaochen Zhao, Hongwen Zhang, and Yebin Liu. Avatarmav: Fast 3d head avatar reconstruction using motion-aware neural voxels. In *ACM SIGGRAPH 2023 Conference Proceedings*, 2023. 3

[43] Ziyi Yang, Xinyu Gao, Wen Zhou, Shaohui Jiao, Yuqing Zhang, and Xiaogang Jin. Deformable 3d gaussians for high-fidelity monocular dynamic scene reconstruction. *arXiv*, 2309.13101, 2023. 2

[44] Wang Yifan, Felice Serena, Shihao Wu, Cengiz Öztireli, and Olga Sorkine-Hornung. Differentiable surface splatting for point-based geometry processing. *ACM Transactions on Graphics (proceedings of ACM SIGGRAPH ASIA)*, 38(6), 2019. 4

[45] Richard Zhang, Phillip Isola, Alexei A Efros, Eli Shechtman, and Oliver Wang. The unreasonable effectiveness of deep features as a perceptual metric. In *CVPR*, 2018. 5

[46] Yufeng Zheng, Victoria Fernández Abrevaya, Marcel C. Bühler, Xu Chen, Michael J. Black, and Otmar Hilliges. I M Avatar: Implicit morphable head avatars from videos. In *Computer Vision and Pattern Recognition (CVPR)*, 2022. 3, 5, 7

[47] Yufeng Zheng, Wang Yifan, Gordon Wetzstein, Michael J. Black, and Otmar Hilliges. Pointavatar: Deformable point-based head avatars from videos. In *Proceedings of the IEEE/CVF Conference on Computer Vision and Pattern Recognition (CVPR)*, 2023. 1, 2, 3, 5, 6, 7, 8, 13

[48] Wojciech Zielonka, Timo Bolkart, and Justus Thies. Instant volumetric head avatars. In *Conference on Computer Vision and Pattern Recognition*, 2023. 1, 2, 3, 5, 6, 7, 8, 11, 12, 13

Supplementary Material
HeadGaS: Real-Time Animatable Head Avatars via 3D Gaussian Splatting

This supplementary material provides further details about HeadGaS, as well as additional results. Section A provides some insights on the learned 3D Gaussians, such as visualization of the learned feature basis as well as a gradual removal of the Gaussians to observe the occluded content. Section B provides more implementation details on the methods used in the ablation of the main paper. Further, we provide some time analysis in Section C. In Section D we show more qualitative results on the novel expression task comparing ours against baselines. Finally, in this supplement we refer the reader to a *demo video* which contains method highlights and a few result sequences.

A. Understanding the learned 3D Gaussians

Basis visualization Since HeadGaS relies on a feature basis for blending, it would be beneficial to understand what this basis is learning. For this purpose, we utilize expression parameters as one-hot vectors to our model and show the generated image alongside the 3DMM mesh corresponding to that expression in Figure S1. The top section of the figure shows two examples on the NBS data [11], using Face Warehouse [5], while the bottom part provides two FLAME [20] based examples from the INSTA data [48]. Note that for the FLAME-based tracking we noticed that the optimized neutral expressions were far from a vector of zeros, therefore we normalized the one-hot expression vectors first, by adding the expression weights of a neutral expression from the training set. Since the Face Warehouse basis is more semantic, *i.e.* every expression element corresponds to a more local and interpretable action, such as winking, or opening mouth in surprise, we observe more drastic changes in this base compared to FLAME. The results show that HeadGaS learns a reasonable feature basis that aligns well with the 3DMM expressions. However, this is limited by the level in which an expression is observed in the training data, *e.g.* for subject 2 from the top we observe that winking does not work quite well (both eyes are closing instead of one) due to this reason.

Gradual removal of Gaussians The purpose of this experiment is to reveal what the intermediate Gaussians in a particular frame represent. This is of interest because the proposed method relies on over-representation, *i.e.* multiple Gaussians will represent certain face areas (*e.g.* lips) and
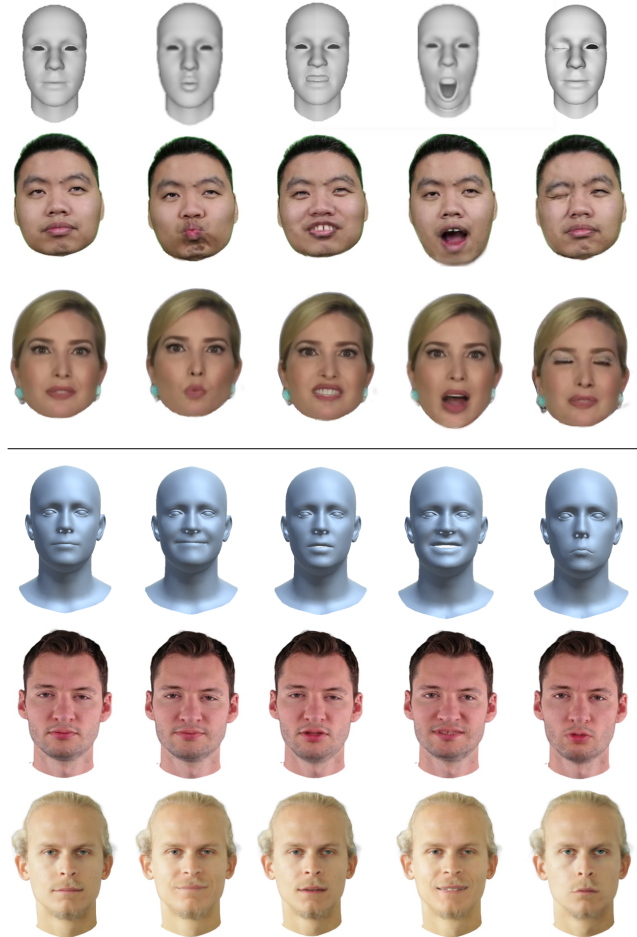

Figure S1. **Learned feature basis visualization.** *Top:* Expression parameters from the Face Warehouse model *Bottom:* Expression parameters from the FLAME model.

they will occasionally become transparent to reveal other areas underneath (*e.g.* teeth) as needed. Therefore we remove the optimized 3D Gaussians gradually, using the camera view as direction, from near to far. Figure S2 shows the original rendering for a given frame as well as the rendering after we have removed the most frontal Gaussians in the mouth area. As expected, we start seeing teeth in the intermediate layers of visibility, as these structures have been observed from other frames (*e.g.* when the person was

original render   render after partial Gaussian removal

Figure S2. Removal of frontal 3D Gaussians reveals underlying structures such as teeth, invisible in this frame, but observed in other frames.

talking or laughing). Additionally, we observe background color (white) when dis-occluding the regions between the nose and the upper lip. This is due to the fact that there is no need to represent the structures underneath, as they are never observed by any frame.

B. Ablation details

This section provides more details on the ablation methods presented and evaluated in the main paper.

Ours w/o MLP   This model does not use learned features for the blending, but rather it blends a basis of colors and opacities directly. In each Gaussian we create these bases as $C \in \mathbb{R}^{B \times 3(k+1)^2}$ and $\alpha \in \mathbb{R}^{B \times 1}$ and use the expression weights to obtain the final color c_i and opacity α_i as a weighted average. Note that summation did not work here, as colors are explicit values and they would add up to high values.

Ours w/ $\Delta(\mu, R)$ This model uses the learned feature basis F of HeadGaS to rather shift the positions μ and transform the rotations R. Thereby we feed the blended feature f_i in to an MLP $\phi'(\cdot)$ that contains the same number of layers and hidden dimensions as $\phi(\cdot)$ from our proposed model. The difference is that, $\phi'(\cdot)$ outputs 3 values of position shift and 4 values of rotation (represented as quaternion) as:

$$\Delta\boldsymbol{\mu}, \boldsymbol{r}_t = \phi'(\boldsymbol{f}_i, \psi(\boldsymbol{\mu})). \tag{7}$$

These outputs are namely used to transform the static parameters of the Gaussian (after converting $\boldsymbol{r}_t$ to a rotation matrix $\boldsymbol{R}_t$) as

$$\boldsymbol{\mu}' = \boldsymbol{\mu} + \Delta\boldsymbol{\mu} \tag{8}$$

and

$$\boldsymbol{R}' = \boldsymbol{R}_t \boldsymbol{R}. \tag{9}$$

Ours w/o blending   This model aims to verify that using the expression parameters as a weight for blending Gaussian features works better than using it as a simple condition to the MLP. Therefore, here we do not have a basis of latent features F. Instead, the expression vector e_i and the encoded position μ are fed directly into $\phi(\cdot)$ to predict the color and opacity. The implementation of the MLP remains the same.

Ours w/o $\mathcal{L}_p$ This model is the same as the proposed HeadGaS and simply has the perceptual loss disabled.

C. Time analysis

Time vs performance   In Figure S3 we visualize the rendering speed in FPS vs image quality (PSNR) for HeadGaS and other baselines on the INSTA data [48]. The radius circles are proportional to training time (smaller is better). Note that the x-axis (FPS) is presented in logarithmic scale. We observe that the proposed method clearly outperforms others in both rendering speed and quality, while the training time is closer to the fastest methods (INSTA).
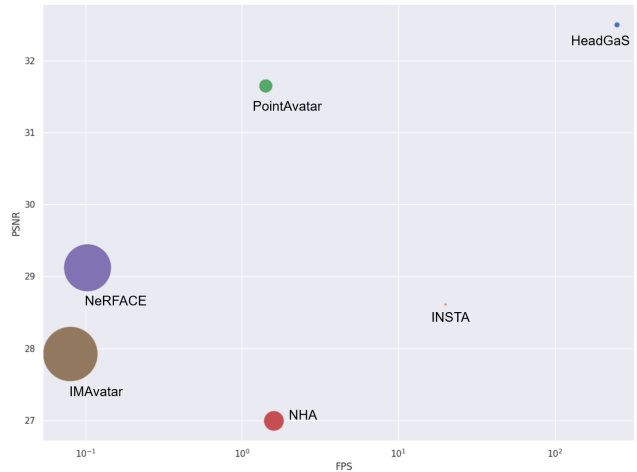

Figure S3. Rendering speed (FPS in logarithmic scale) vs PSNR plot comparing different methods on the INSTA dataset. The circle radius represents training time.

Rendering time vs image size   In Figure S4 we plot our models relationship between rendering time and image resolution. For each subject we render our models in 3 different resolutions, namely 512^2, 1024^2 and 2048^2 and collect the run-time statistics. The number of Gaussians range between 21k and 37k, which is one of the main factors affecting the rendering time. The resulting mean rendering time for each resolution is namely 0.004, 0.005 and 0.0086, *i.e.* the rendering time only doubles when we increase resolution by a factor of 4 in both dimensions (*i.e.* 16× more
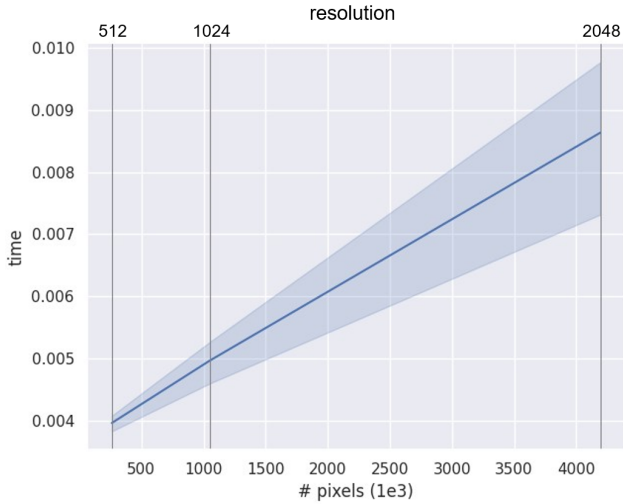
pixels).

Figure S4. Rendering time with respect to image resolution for HeadGaS on the INSTA dataset. We show the statistics of all subjects, with number of Gaussians ranging from 21k to 37k.

Ablation on number of 3D Gaussians and rendering time   In addition to the image quality metrics evaluated in the main paper, we compare our different ablation models in terms of rendering time and number of Gaussians in Table S1. We notice that the proposed HeadGaS (Ours) results in significantly less Gaussians compared to other models while being the fastest to render. Interestingly, the model that blends explicit parameters directly (Ours w/o MLP) is still slower than ours, despite not employing an MLP computation due to its large number of Gaussians. Another interesting observation is that, even though HeadGaS relies on over-representation, it still leads to significantly less Gaussians compared to the alternative model that transforms Gaussians (Ours w/ $\Delta(\mu, R)$). We believe this is due to the fact that the proposed model is more effective and easier to learn, and therefore it leads to the most efficient representation of space compared to other variants.

Method	# Gaussians ↓	Time (s) ↓	PSNR ↑
Ours w/o blending	135k	0.008	29.38
Ours w/ $\Delta(\mu, R)$	234k	0.019	29.83
Ours w/o MLP	295k	0.010	32.08
Ours	**28k**	**0.004**	**32.50**

Table S1. Ablation methods compared in terms of number of optimized 3D Gaussians and per-frame rendering time. Our method leads to the lowest number of Gaussians (*i.e.* most efficient coverage of space) while having the best PSNR.

D. Additional qualitative results

We provide additional qualitative results comparing HeadGaS against the most recent baselines [11, 47, 48] in Figure S5 and Figure S6. We observe that generally our model renders images with less artifacts, higher similarity to the ground truth expression, more noticeable reflecting glasses and skin specularities (Figure S5, row 2).
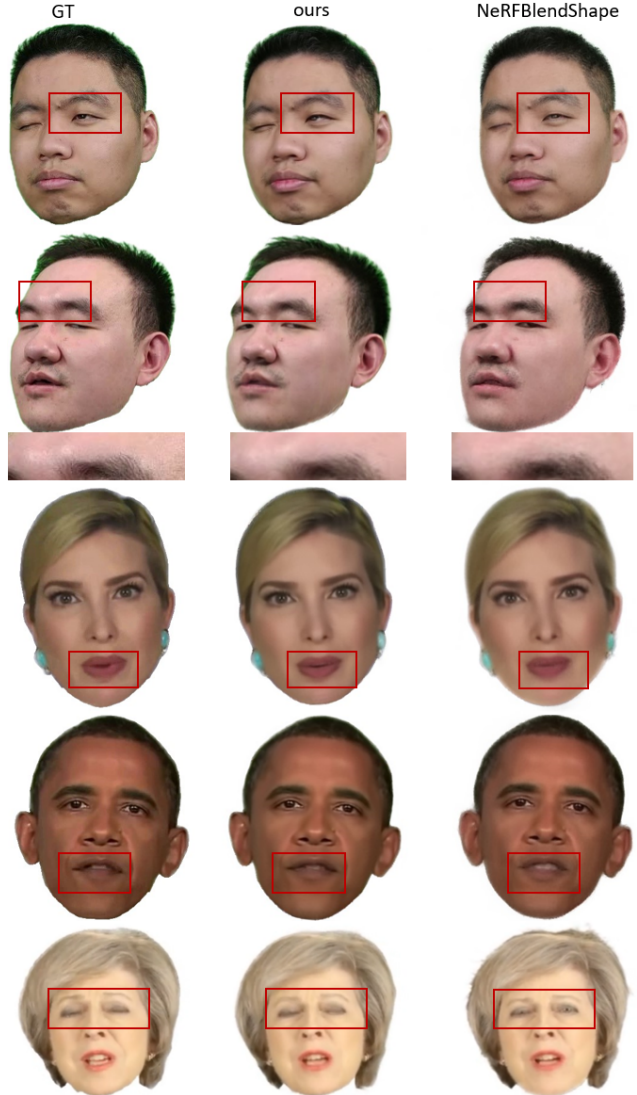

Figure S5. Additional qualitative results on the NBS data. *Left:* Ground truth, *Center:* HeadGaS (ours), *Right:* NeRFBlendShape.
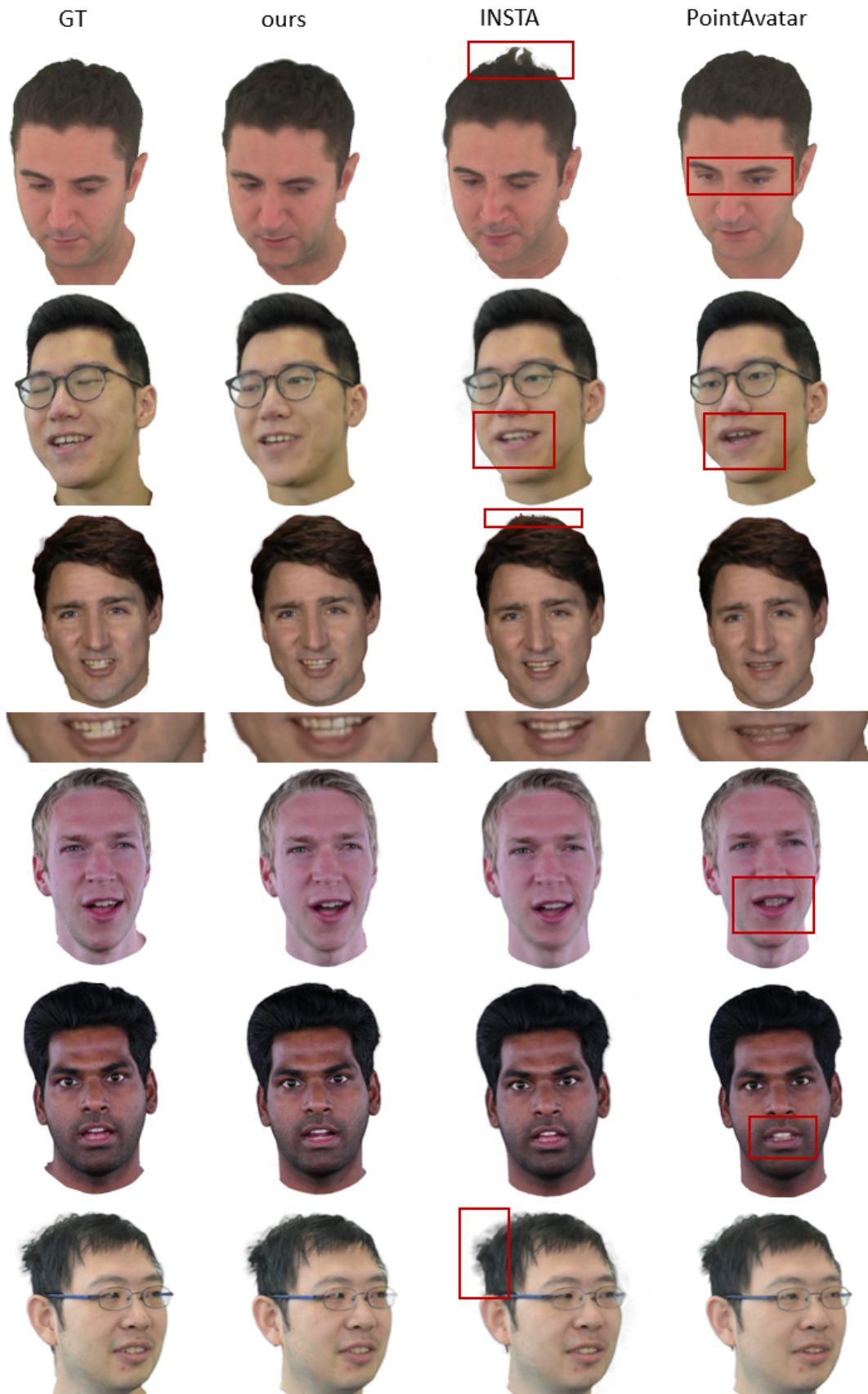
13

Figure S6. Additional qualitative results on the INSTA data. From left to right: Ground truth, HeadGaS (ours), INSTA and PointAvatar.